

A wide-field spectroscopic survey of the cluster of galaxies Cl0024+1654

I. The catalogue*

Oliver Czoske¹, Jean-Paul Kneib¹, Geneviève Soucail¹, Terry J. Bridges² **, Yannick Mellier^{3,5}, and
Jean-Charles Cuillandre^{4,5}

¹ Observatoire Midi-Pyrénées, UMR5572, 14 Av. Edouard Belin, 31400 Toulouse, France

² Institute of Astronomy, Madingley Road, Cambridge, CB3 0HA, UK

³ Institut d'Astrophysique de Paris, 98bis Bd. Arago, 75014 Paris, France

⁴ CFHT Corporation, P.O. Box 1597, Kamuela, Hawaii 96743, USA

⁵ Observatoire de Paris, DEMIRM, 61 Av. de l'Observatoire, 75014 Paris, France

Received too late, Accepted even later

Abstract. We present the catalogue of a wide-field CFHT/WHT spectroscopic survey of the lensing cluster Cl0024+1654 at $z = 0.395$. This catalogue contains 618 new spectra, of which 581 have identified redshifts. Adding redshifts available from the literature, the final catalogue contains data for 687 objects with redshifts identified for 650 of them. 295 galaxies have redshifts in the range $0.37 < z < 0.41$, i. e. are cluster members or lie in the immediate neighbourhood of the cluster. The area covered by the survey is $21 \times 25 \text{ arcmin}^2$ in size, corresponding to $4 \times 4.8 h^{-2} \text{ Mpc}^2$ at the cluster redshift. The survey is 45% complete down to $V = 22$ over the whole field covered; within 3 arcmin of the cluster centre the completeness exceeds 80% at the same magnitude. A detailed completeness analysis is presented. The catalogue gives astrometric position, redshift, V magnitude and $V - I$ colour, as well as the equivalent widths for a number of lines. Apart from the cluster Cl0024+1654 itself, three other structures are identified in redshift space: a group of galaxies at $z = 0.38$, just in front of Cl0024+1654 and probably interacting with it, a close pair of groups of galaxies at $z \sim 0.495$ and an overdensity of galaxies at $z \sim 0.18$ with no obvious centre. The spectroscopic catalogue will be used to trace the three-dimensional structure of the cluster Cl0024+1654 as well as study the physical properties of the galaxies in the cluster and in its environment.

Key words. galaxies: clusters: Cl0024+1654 – cosmology: observations – cosmology: large-scale structure of the Universe

1. Introduction

Clusters of galaxies are increasingly viewed not as simple isolated and relaxed systems but as embedded in and connected to the general large-scale structure in the Universe. This view of clusters in a larger context has consequences for the interpretation of cluster galaxy populations, cluster dynamics and mass estimates.

Clusters of galaxies grow by continuously accreting galaxies and groups of galaxies from the surrounding field, mostly along filamentary structures. In the process, galax-

ies are transformed from the predominantly blue, actively star-forming, spiral population characteristic of the field to the red, passive and elliptical population characteristic of the inner and denser regions of clusters (Dressler 1980, Abraham et al. 1996, Balogh et al. 1998). Cluster galaxy populations evolve with redshift: rich clusters at high redshift contain a larger fraction of blue galaxies than local ones (Butcher & Oemler 1978, 1984; Cl0024+1654 is an example of a “Butcher-Oemler” cluster). The exact nature of the interaction of infalling galaxies with the cluster environment (hot intra-cluster medium, tidal gravitational field) and its influence on the morphology of galaxies, their gas content and star-formation rates (as measured by galaxy colours and spectral type) are as yet ill-understood; hence the interest in investigating the “in-fall region” beyond $\sim 1 h^{-1} \text{ Mpc}$ distance from the cluster centre, where the transition from field to cluster galax-

Send offprint requests to: O. Czoske, e-mail: oczoske@ast.obs-mip.fr

* Based on observations obtained with the Canada–France–Hawaii Telescope and the William–Herschel Telescope.

** Present address: Anglo–Australian Telescope, PO Box 296, Epping NSW 1710, Australia

ies is taking place. The advent of new wide-field CCD mosaic cameras available on a number of large telescopes (e. g. CFHT, CTIO, Subaru, ESO2.2m) makes it possible to obtain photometric and morphological information on 1 - 10 Mpc scales around the cluster centres. However, wide-field investigation of clusters demands both imaging and spectroscopic observations. Individual spectra of galaxies describe their spectral energy distribution and provide their redshift, which is indispensable to produce a catalogue of cluster members with radial velocity and information regarding their stellar content and star formation history. At present there is only a limited number of clusters with more than ~ 200 spectroscopically identified member galaxies (e. g. Abraham et al. 1996), and especially at high redshift ($z \gtrsim 0.2$) spectroscopically well-studied clusters become very rare, mostly due to the fact that contamination by field galaxies increases rapidly with redshift.

The fact that clusters are not isolated systems also raises questions concerning the traditional ways of estimating masses of clusters of galaxies through different mass estimators: gravitational lensing analyses, kinematical analyses from redshifts of cluster member galaxies and X-ray observations.

Gravitational lensing is sensitive to the total integrated mass along the line-of-sight from the observer to the lensed sources, weighted by the appropriate combination of angular size distances between observer, lens and source (e. g. Schneider, Ehlers & Falco 1992, Bartelmann & Schneider 2001). In the presence of massive structures other than the cluster along the line of sight, the mass derived from gravitational lensing overestimates the mass of the cluster proper. Large spectroscopic surveys provide additional information needed to correctly interpret the lensing analysis in this case. Metzler et al. (2000) investigate the influence of the presence of filaments and groups of galaxies in the vicinity of a cluster on weak lensing estimates of the cluster mass and find that significant overestimates (up to a factor 1.5 to 2) are possible and even likely. Similar investigations with comparable results were conducted by Cen et al. (1997) and Reblinsky et al. (1999).

A similar bias should be expected to affect measurements of velocity dispersions: if foreground or background groups of galaxies in the immediate neighbourhood of the cluster are added into the redshift histogram, but are not resolved and recognized as separate entities, the velocity dispersion of the cluster itself will be overestimated. Generally only 30 to 50 member galaxies are used to estimate the line-of-sight velocity dispersion (and virial cluster mass; see e. g. the large compilations of Girardi et al. 1998 and Girardi & Mezzetti 2000). Furthermore, the measured redshifts are generally concentrated within a relatively small region within a projected radius of $\sim 500 h^{-1}$ kpc of the cluster centre. Whereas one can argue that these numbers might be sufficient for relaxed clusters with regular spatial and velocity distributions, the various derived estimates will contain large systematic errors if unresolved substructures are present. What can be ob-

tained from redshift surveys is a galaxy number density weighted line-of-sight velocity dispersion averaged along the line-of-sight. With a sufficiently large number of cluster member redshifts it is possible to measure the variation of the line-of-sight velocity dispersion with projected distance from the cluster centre (Carlberg et al. 1997), but determination of even more detailed information on the dynamical status (e. g. velocity anisotropy profile) of a cluster requires a forbiddingly large number of redshifts (e. g. Merritt 1987).

Clearly, combining information coming from gravitational lensing (weak and strong), the X-ray emission from the hot intra-cluster gas, the Sunyaev-Zeldovich effect and the galaxy velocity distribution is the best way to arrive at secure mass estimates for clusters of galaxies (see e. g. Castander et al. 2000). This is now possible for several cases. Of particular interest are clusters for which a significant discrepancy between different mass estimates is found. One such cluster is the well-known lensing cluster Cl0024+1654¹. About 100 redshifts of galaxies in this cluster were obtained by Dressler & Gunn (1992) and Dressler et al. (1999), resulting in a velocity dispersion of $\sigma \simeq 1300 \text{ km s}^{-1}$, which is consistent with mass estimates derived from the spectacular arc system in the cluster centre (Kassiola, Kovner & Fort 1992, Smail et al. 1996, Tyson et al. 1998, Broadhurst et al. 2000). Cl0024+1654 was among the first clusters in which a coherent shear signal due to weak lensing was found (Bonnet et al. 1994). A crude mass estimate from this analysis was consistent with the strong lensing and kinematical estimates. In addition to the signal due to Cl0024+1654 itself, Bonnet et al. (1994) also found a coherent signal to the north-east of the cluster centre in an area where no obvious galaxy overdensity could be seen. The X-ray luminosity of Cl0024+1654 on the other hand is unusually low for a cluster of this velocity dispersion, and mass estimates from the X-ray observations are a factor of two to three lower than the lensing and kinematical estimates (Soucail et al. 2000).

In order to better understand the dynamics of Cl0024+1654 and how it is embedded in the surrounding large-scale structure, we have conducted a wide-field spectroscopic survey at the Canada-France-Hawaii Telescope (CFHT) and the William Herschel Telescope (WHT) from 1992 to 1996. In this paper we present the catalogue of the galaxies observed for this survey. Section 2 summarizes the photometric and spectroscopic observations. The data reduction and analysis are presented in Section 3. Section 4 discusses some interesting global results of the survey and describes some structures found in the redshift distribution that are not directly related to the cluster Cl0024+1654. A summary is given in Section 5. A detailed analysis of the dynamics of the cluster itself and its

¹ This cluster is commonly called Cl0024+1654, although the common Internet databases, such as NED (<http://nedwww.ipac.caltech.edu>), list it as ZwCl0024.0+1652 as it originally appeared in Zwicky (1965).

environment as well as the spectral properties of its member galaxies will be the subject of a forthcoming paper (Czoske et al. 2001).

Throughout this paper we use a Hubble constant $H_0 = 100 h^{-1} \text{ km s}^{-1} \text{ Mpc}^{-1}$, $\Omega_M = 1$ and $\Omega_\Lambda = 0$, which gives a physical scale of $3.195 h^{-1} \text{ kpc arcsec}^{-1}$ at the cluster redshift.

2. Observations

2.1. Imaging

We will use photometric results from two broad-band images in the analysis of the spectroscopic survey presented in this paper.

On 26 September 1995, we obtained an I-band image using the UH8k camera (Luppino, Metzger & Miyazaki 1995) on CFHT. The I-band image was reduced chip by chip, i. e. the final result is in the form of eight individual images, one for each chip of the camera. The final images were obtained as the mean of 10 exposures of 1200 s each, using sigma clipping (2.5σ above the mean level and 4σ below) to reject hot pixels and cosmic ray hits, and have very good seeing of $0''.7$ FWHM; however, the background is marred by stray light, presumably due to the bright star 47 Psc ($V = 5.1$, spectral type M3) at $\sim 50'$ distance from the centre of Cl0024+1654, although outside the field of view of the UH8k. The I-band photometric catalogue was obtained from the individually stacked chips using the SExtractor package (Bertin & Arnouts 1996) with a threshold of 1.5σ and a minimum detection area of 5 pixels. The catalogue contains more than 4×10^4 objects over a field of about $28 \times 28 \text{ arcmin}^2$, the limiting magnitude is $I \sim 24$. Unless otherwise noted, we use total magnitudes as given by SExtractor's `MAG_BEST`. The internal errors on the I-band magnitudes (as given by SExtractor) are smaller than 0.05 for $I < 22.7$ (0.01 for $I < 20.7$). Note that due to the chip-wise reduction of the I-band image, the gaps between the chips (of typical width 5-10 arcsec) were not filled in during stacking and the photometric catalogue contains no objects from these regions.

On 15 November 1999 we obtained a 3600 s V-band image using the CFH12k camera (Cuillandre et al. 2000) on CFHT (Figs. 1 and 4a-4h). The six individual exposures were bias and flat-field corrected in the standard way using the MSCRED package under IRAF². The exposures were then registered onto the Digital Sky Survey³ (DSS) image of the field and median combined. The final image, a mosaic of all 12 chips with all the inter-chip gaps filled in, has $\sim 0''.7$ seeing (FWHM). The V-band photometric catalogue obtained from this image contains $\sim 3.7 \times 10^4$ objects on a field of $\sim 42 \times 28 \text{ arcmin}^2$. The internal errors on the V-band magnitudes are smaller than 0.05 for

$V < 23.3$ (0.01 for $V < 21.1$). The limiting magnitude is $V \sim 25$.

In order to obtain colour information aperture magnitudes were measured in 14 pixel ($2''.8$) diameter apertures for the V- and I-band images. This diameter is sufficiently large compared to the seeing FWHM to enclose most of the light from the object under consideration and small enough to avoid contamination by neighbouring objects in crowded regions like the cluster centre. The objects were then matched up using a polynomial transformation of the I-band image coordinates onto the system of the V-band image. The centres of the two images coincide to within 40 arcsec, so that the overlapping region covers virtually the whole UH8k field. Note that the gaps from the I band image show up in the colour-magnitude catalogue as well. The resulting colour-magnitude catalogue contains $\sim 2.1 \times 10^4$ objects with errors on the colours of smaller than 0.05 for $V < 23.3$ (0.01 for $V < 21.1$). Star-galaxy classification over a sub-region of the colour-magnitude plane (as relevant for the present paper) will be described in Sect. 3.5.

A more detailed description of the photometric catalogue (including star-galaxy separation over the whole colour-magnitude plane) is given in Mayen et al. (2001) who use this catalogue to investigate the depletion of background galaxies due to the gravitational lens effect of Cl0024.

2.2. Spectroscopy

Spectra were obtained using multi-slit spectroscopy during three observing runs at CFHT and one at WHT. Table 1 shows the observing log.

Candidates for all the runs (except for run 1) were selected from a V-band mosaic obtained at the ESO New Technology Telescope (NTT) on 17/18 October 1993, with the primary selection criterion being $V_{\text{NTT}} < 23$. The seeing on this image was rather poor, $\sim 1''.7$ FWHM. In order to reduce contamination by stars, the preparatory shallow R-band images were carefully examined during all the CFHT runs; for runs 3 and 4, we took additional advantage of the excellent seeing of the deep UH8k I-band image.

All the CFHT observations were done with the Multi-Object Spectrograph (MOS, Le Fèvre et al. 1994) with the O300 grism. The cameras used during each run and the corresponding pixel scales and dispersions are listed in Table 1. Two to five exposures per mask were obtained, depending on the magnitudes of the selected objects in each mask.

Band-limiting filters, chosen such that prominent spectral features (for instance the Ca I H/K lines blueward of the 4000 Å break) fall into the band at the redshift of interest, allow stacking of several rows of spectra on one mask, thus increasing the number of spectra observable in a given time. This strategy has been successfully employed by e. g. Yee et al. (1996, 2000). However, spectra covering

² IRAF is distributed by the National Optical Astronomy Observatories, which are operated by the Association of Universities for Research in Astronomy, Inc., under cooperative agreement with the National Science Foundation.

³ <http://archive.stsci.edu/dss/>

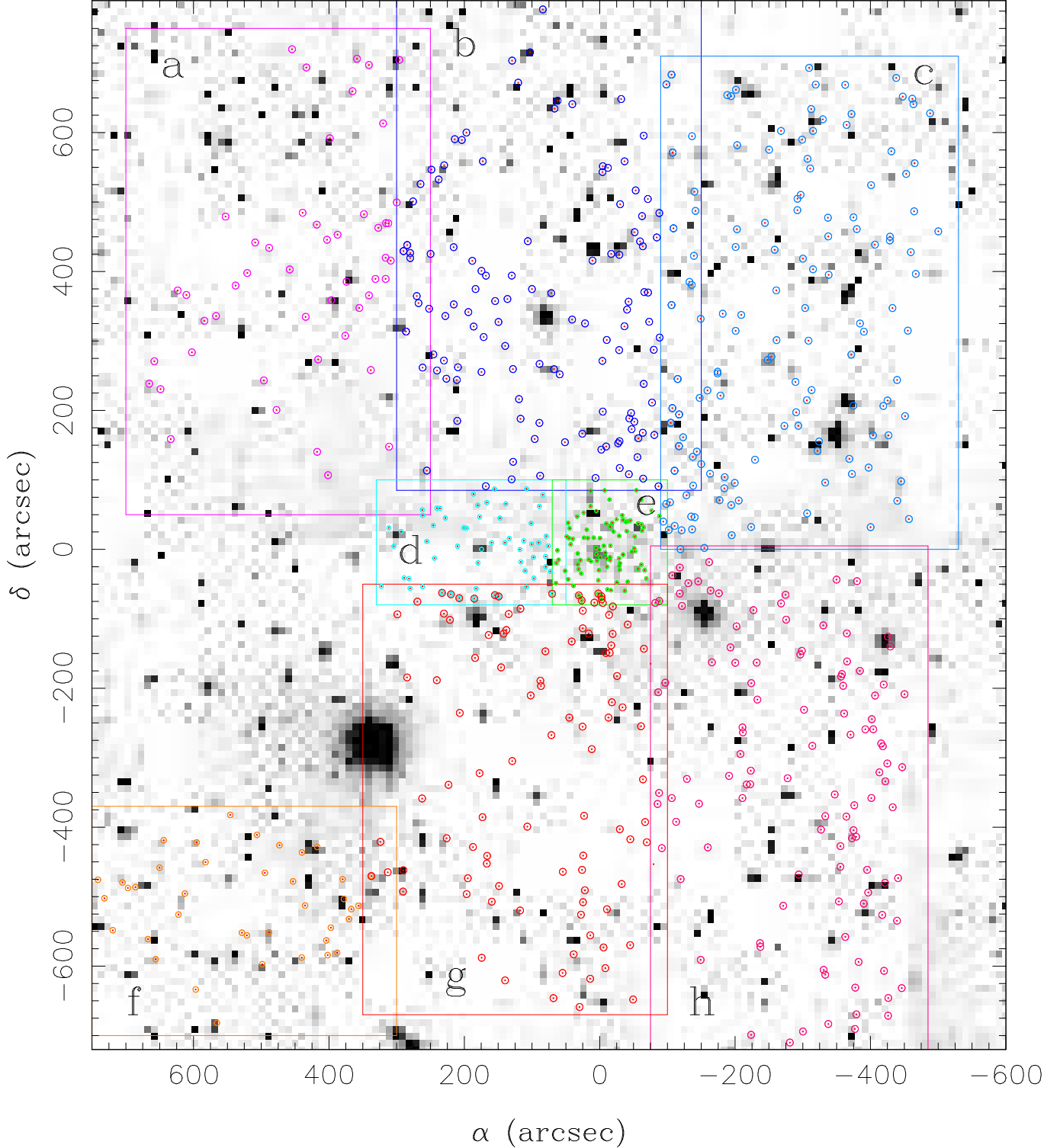


Fig. 1. $22' \times 25'$ section of the CFH12k V-band image showing the distribution of the objects in our spectroscopic sample. Expanded views of the marked regions are shown in Figs. 4a–4h as indicated in the image. The coordinates given are right ascension and declination relative to $\alpha_{2000} = 00^{\text{h}}26^{\text{m}}35^{\text{s}}.70$, $\delta_{2000} = 17^{\circ}09'43''.06$.

a larger range of wavelengths provide more secure redshift determinations since more absorption and emission lines can be taken into account. This is particularly important in the presence of artifacts caused by insufficient removal of cosmic ray hits. In the case of Cl0024+1654 at

$z = 0.395$, the 4000 \AA break roughly coincides with the strong sky emission line $[\text{O I}] \lambda 5577$, so that insufficient subtraction of the sky line might cause a problem in the redshift determination if only a limited wavelength band were available. Also, covering a wide wavelength range is

essential in order to derive spectral types for the galaxies and analyse in detail the spectral properties of the cluster members. For these reasons we did not use band-limiting filters and the usable wavelength range was typically 4500–8500 Å, depending on signal-to-noise ratio and the quality of the sky subtraction at the red end of the spectral range, where the sky emission is dominated by molecular bands.

The observations at WHT were made with the Low Dispersion Survey Spectrograph (LDSS-2, Allington-Smith et al. 1994), the med/blue grism and the Loral LOR1 detector. The usable wavelength range was 4000–7500 Å, somewhat bluer than for the MOS observations. All the LDSS-2 masks were covered by two exposures each.

We used 1'' wide slits throughout, resulting in a resolution of ~ 13 Å, except for run 1 where the slit width used was 1''.5 with a correspondingly worse resolution of ~ 20 Å.

3. Data reduction and analysis

3.1. Reduction of spectroscopic data

The spectra were reduced using the semiautomatic package MULTIRED (Le Fèvre et al. 1995) which in turn uses standard IRAF tasks and treats each slit separately. The spectral images were de-biased and flat-field corrected in the standard way. A low-order (mostly linear) polynomial fit to the sky emission in the spatial direction was then subtracted for each individual exposure. During the fit most of the cosmic ray hits in the sky region of the spectral images were taken care of by a sigma-rejection algorithm (pixels with deviations of more than $\pm 2\sigma$ from the fit were rejected before refitting); nevertheless insufficiently rejected cosmics occasionally survived the fit to produce fake absorption features in the object spectrum.

Geometric distortions cause the true spatial/dispersion directions to deviate from the row/column directions of the CCD chip, especially at the edges of the field. Since sky fitting was done row-wise (column-wise for the WHT data), sky emission lines tend to be imperfectly subtracted. Isolated emission lines (in particular [O I] $\lambda 5577$, which roughly coincides with the 4000 Å break for galaxies at the redshift of Cl0024+1654) could simply be masked for the subsequent analysis of the spectrum, but the usable wavelength range in the red was effectively limited by the molecular band emission from the sky.

The individual exposures were then averaged into the final two-dimensional spectrum. In those cases where more than two exposures per mask were available, the highest pixel value was rejected, thus accounting for cosmic ray hits. The small number of exposures per mask made cosmic ray rejection difficult and imperfect. A cosmic ray hit on the object spectrum resulted in a fake emission feature, a hit in the sky area in a fake absorption feature. However, as argued in Section 3.2, cosmics do not in general influence the redshift determination. Finally, variance-weighted one-dimensional spectra were extracted from the combined spectral images, wavelength calibrated

using lamp spectra (He/Ar at CFHT, Cu/Ar at WHT) and approximately flux-calibrated with long-slit spectra from spectro-photometric standard stars (listed in Table 1).

The wavelength calibration spectra were extracted using a straight trace (following the column/row direction of the CCD), unlike the corresponding object spectra, where the trace followed the flexure introduced by geometric camera distortions. We verified that this causes only negligible errors by re-calibrating several spectra with strong flexure with calibration spectra extracted using the same trace as for the object spectra.

We finally performed a check on the wavelength calibration by extracting three spectra per mask without sky subtraction and measuring the position of prominent sky lines using the calibration from the lamps. For the WHT masks this revealed systematic shifts, which are due to the fact that the lamp spectra were not taken immediately before or after the science exposures. The positioning of the masks in the mask holder was therefore not identical during lamp and science exposures. These systematic shifts translate to $\sim 10^{-3}$ in terms of redshift and a correction for each mask was applied to all the redshifts determined from this mask. No such systematic effect was found for the CFHT masks.

Seven example spectra and the V-band images for the corresponding objects are shown in Fig. 2.

3.2. Redshift determination

Since a large fraction of the spectra in our sample have rather low signal-to-noise ratio, we decided to identify redshifts by eye, which is better at finding real absorption and emission lines amongst noise than automatic redshift identification techniques. Also, fake emission and absorption features due to cosmics could be identified this way by simply checking the original two-dimensional spectral images. All redshifts were identified by one of us (OC for runs 2-4, GS for run 1) and checked by at least one other member of the team. The redshifts (runs 2-4 only) given in Table 4 carry a flag which indicates a (somewhat subjective) level of confidence that the redshift identification is correct. “Secure/A” redshifts were determined from spectra where emission lines and/or several absorption lines are clearly seen, “uncertain/D” redshifts are based on a tentative identification of a single line or possibly several weak absorption lines, and “probable/B” and “possible/C” indicate intermediate levels of confidence.

In order to obtain a more objective estimate of the *measurement* (as opposed to *identification*) error of our redshifts, we used the cross-correlation technique implemented in the task XCSAO in the IRAF package RVSAO (Kurtz & Mink 1998). In all cases, the by-eye redshift identification was fed to XCSAO as the initial redshift estimate and the allowed redshift range was restricted to about $\pm 5\%$ around this redshift. In this sense, XCSAO was

Table 1. Log of the spectroscopic observing runs.

#	Date	Instrument	CCD	Grism	N_{masks}	Exp. time (ksec)	Pixel (μm)(arcsec)	Disp. (\AA /pix)	Std. star
1	24–27/08/92	CFHT/MOS	SAIC1	O300	2	4.5 – 7.5	18 0.377	4.31	Feige 110
2	24–27/08/95	CFHT/MOS	Loral-3	O300	6	6.6 – 15.6	15 0.314	3.69	Wolf 1346
3	12–15/09/96	WHT/LDSS-2	LOR1	med/blue	9	5.4 – 7.2	15 0.357	3.30	HZ4
4	11–13/11/96	CFHT/MOS	STIS-2	O300-1	3	6.6 – 8.1	21 0.440	5.03	Hiltner 600

Table 2. Comparison of multiply observed objects. The first three lines give numbers determined from objects observed twice during the same runs, the last three lines compare different runs. All the redshift differences are given in units of 10^{-4} . The numbers of the observing runs are those given in Table 1.

Runs	N	all qualities		“secure/A” only	
		$ z_1 - z_2 $	$(z_1 - z_2)$	N	$ z_1 - z_2 $
2 – 2	19	8.2	—	19	8.2
3 – 3	6	4.8	—	4	5.8
4 – 4	9	6.6	—	7	5.4
2 – 3	28	14.0	6 ± 19	26	10.6
2 – D99	24	12.8	2 ± 19	22	9.6
3 – D99	28	10.0	-6 ± 16	25	13.4

forced to recover our redshift identification and we only used XCSAO’s error estimate.

For large values of the correlation parameter, $R > 3$ (Kurtz & Mink 1998), we find that XCSAO reproduces our input redshifts very well. The mean deviation between by-eye redshift and XCSAO redshift is $(z_{\text{eye}} - z_{\text{xcsao}}) = -0.00018$ with a scatter of 0.00037, corresponding to 80 km s^{-1} at the redshift of Cl0024. However, only 107 of our spectra achieve $R > 3$ and the redshift distribution of these is not representative of the redshift distribution of the total sample, low-redshift objects being more reliably identified than objects at the cluster redshift or beyond. XCSAO assigns an individual error estimate to each redshift, based on the width of the peak in the correlation function. For $R > 3$, the median of the distribution of this error is at ~ 0.0003 (43 km s^{-1}), with the bulk of error estimates at < 0.0005 .

However, these error estimates are only useful for our “best” spectra. In order to get a more reliable error estimate for all the spectra we can compare redshifts determined from multiple observations either during the same run, when the same object appears on different masks, or during different observing runs. The results of this inter-comparison are shown in Table 2 for those pairs of runs with useful number N of pairs: The mean absolute differences between the redshifts are of order 1×10^{-3} , with no marked difference between the values determined for all quality codes or “secure/A” redshifts only. We note that the slits at the “southern” ends of the WHT masks were consistently of rather poor quality, in the sense that

the slit edges become quite rugged. Redshifts from these slits are therefore less accurate than those from the central and “northern” parts of the WHT masks or from the observing runs at CFHT. Taking this fact into account we estimate that most of our redshifts are accurate to about $\sim 1 \times 10^{-3}$. The majority of our spectra were obtained during observing runs 2 and 3; comparing the redshifts of objects observed during both these runs we find that the systematic shift $(z_1 - z_2)$ between the observations is consistent with zero.

Finally we compare in Fig. 3 the redshifts for those 54 objects that were observed both by us and by Dressler et al. (1999). For the majority of these objects the redshift measurements agree very well, however, there are five clear misidentifications, with redshift deviation of more than 0.01 ; these cases are discussed in detail in Sect. 3.4. Object 523 deviates by more than 3σ if the five misidentifications are dropped from the sample, so we exclude this object as well. The remaining 48 common objects have a mean redshift deviation of $z_{\text{D99}} - z_{\text{our}} = -0.0003$ with a root mean square (RMS) scatter of $\sigma = 0.0015$. The rms scatter is consistent with the estimate for our redshift error estimate of 10^{-3} , assuming that the redshifts given by Dressler et al. (1999) have similar accuracy. Again, there is no evidence for a systematic shift.

3.3. Spectroscopic measures

We measured equivalent widths for [O II] $\lambda 3727$, [O III] $\lambda \lambda 4959, 5007$, $\text{H}\alpha$ (where within the wavelength range), $\text{H}\beta$ and $\text{H}\delta$, as well as the strength of the 4000\AA break. [O III], $\text{H}\alpha$ and $\text{H}\beta$ were measured semi-automatically, i. e. the continuum level was placed by visual inspection and the line integration limits were fixed at the values given in Table 3. The integration ranges for [O III] and $\text{H}\beta$ are the same as those used by Dressler & Shectman (1987); the range for $\text{H}\alpha$ is taken from Couch et al. (2000) and does not include the neighbouring [N II] line.

[O II] and $\text{H}\delta$ are important indicators of ongoing (Kennicutt 1992) and recently terminated (Abraham et al. 1996) star formation within galaxies and in particular provide essential information on the interaction of newly accreted galaxies with the cluster environment. We therefore adopted a more accurate way to determine the equivalent widths and in particular to estimate a level of significance for the strengths of these lines. We define our

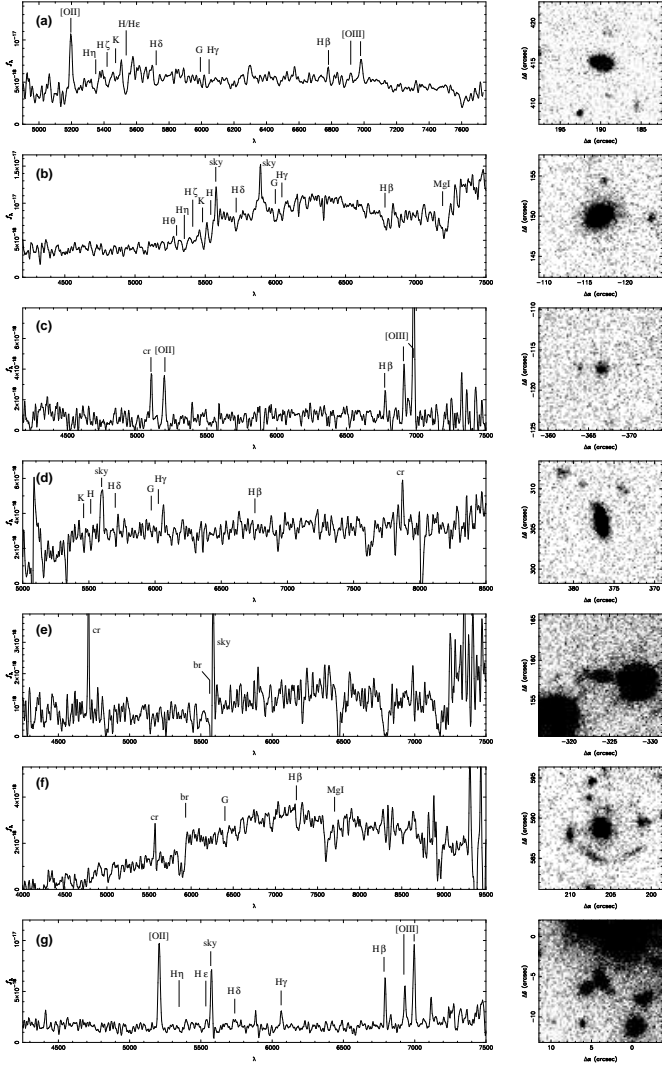


Fig. 2. Example spectra and corresponding 15×15 arcsec² sections from the CFH12k V-band image. The catalogue entries for these objects are listed at the top of Table 4. Spectra (a) and (d) are from observing run 2 (CFHT), spectra (b), (c), (e) and (g) from run 3 (WHT), and spectrum (f) is from run 4 (CFHT). Spectra (a), (b) and (c) are examples of spectra with “secure/A” redshifts based on a large number of emission and/or absorption lines. Spectrum (d) is an example of a “probable/B” redshift and spectrum (e) of an “uncertain/D” redshift, based on the 4000 Å break only. Spectrum (f) is for the central galaxy of the northern group at $z \sim 0.495$, discussed in Sect. 4. Spectrum (g), finally, is for a very blue cluster member near the centre of Cl0024+1654, showing almost the complete Balmer series in emission. Cosmic ray hits are marked “cr”, sky emission lines by “sky”. Note that the wavelength ranges are different in each panel.

equivalent widths so that they are *positive* for emission lines:

$$W_\lambda = \sum_{i=1}^{N_{\text{int}}} \frac{f_i - \bar{f}_c}{\bar{f}_c} \Delta\lambda = \sum_{i=1}^{N_{\text{int}}} \frac{f_i}{\bar{f}_c} - N_{\text{int}} \Delta\lambda \quad , \quad (1)$$

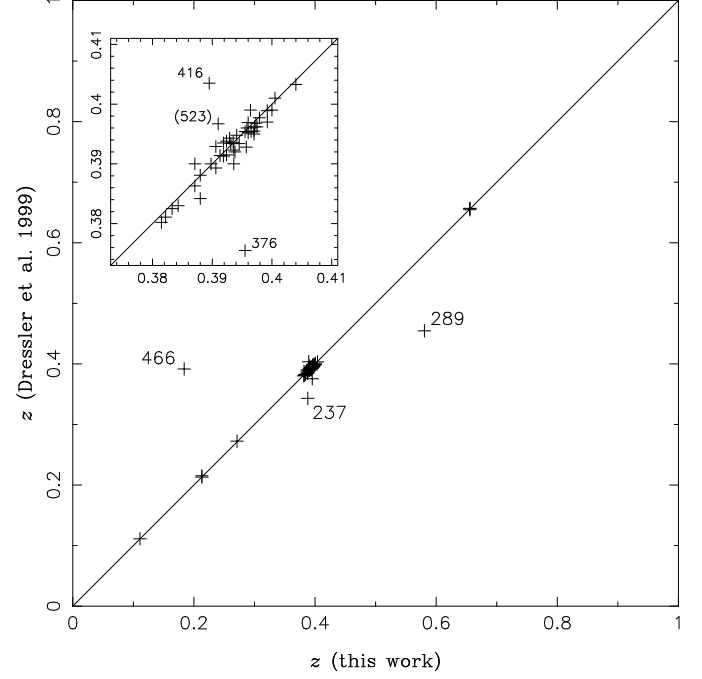


Fig. 3. Comparison of redshift measurements for objects observed both by us and by Dressler et al. (1999). The large panel shows the full samples, the inset is a blow-up of the cluster region. Five clear misidentifications and one 3σ drop-out are labeled with their numbers in the spectroscopic catalogue. The sizes of the symbols in the inset correspond to half our redshift error estimate of $\pm 1 \times 10^{-3}$.

where f_i is the flux in pixel i , N_{int} the number of pixels in the integration range, and $\Delta\lambda$ is the wavelength dispersion in Å/pixel. The continuum level \bar{f}_c was estimated as the mean value within two wavelength intervals on either side of the line; pixels with values more than 3σ away from the mean level were iteratively rejected in order to avoid cosmic ray hits in the continuum region. The automatic measurement of the continuum level makes it possible to estimate an error on the corresponding equivalent widths, thus allowing an assessment of the detection significance of the line. For this purpose we model the noise as Poisson-distributed photon noise. This allows us to relate the variances on f_i and \bar{f}_c to the single-pixel signal-to-noise ratio at flux level \bar{f}_c , $S/N = \bar{f}_c/\sigma_c$ using the usual Poisson scaling $\sigma^2 \propto f$ and $\sigma(\bar{f}_c)^2 = \sigma_c^2/N_c$ when averaged over N_c pixels. Adding the errors due to f_i and \bar{f}_c in quadrature we thus obtain:

$$\sigma_{W_\lambda}^2 = \left(\frac{S}{N}\right)^{-2} \left[(W_\lambda + N_{\text{int}} \Delta\lambda) \Delta\lambda + \frac{(W_\lambda + N_{\text{int}} \Delta\lambda)^2}{N_c} \right]. \quad (2)$$

Here the first term is due to the line integration and the second to the determination of the continuum level.

In the case of [O II], the signal-to-noise ratio S/N was determined between 3560 Å and 3680 Å, a region which

Table 3. Wavelength ranges for equivalent width measurements. All the wavelengths are given in Å (“i/a” — interactive placement of continuum level).

	λ_{cent}	line	blue cont.	red cont.
[O II]	3727	3713–3741	3653–3713	3741–3801
[O III]	5007	4997–5017	i/a	i/a
H α	6563	6556–6570	i/a	i/a
H β	4861	4851–4871	i/a	i/a
H δ	4103	4088–4116	4030–4082	4122–4170
break	4000	–	3750–3950	4050–4250
S/N	–	4050–4250	–	–

is largely free from absorption lines. For H δ , the signal-to-noise ratio was measured in the range 4050 Å to 4250 Å, where the line itself was excised between 4085 Å and 4115 Å. The latter S/N was measured for every spectrum as a global indicator of the quality of the spectrum. The integration ranges correspond to those used by Abraham et al. (1996). For H δ we used their “narrow” range.

The strength of the 4000 Å break is given as the ratio of the total flux in the range $4050 \text{ \AA} < \lambda < 4250 \text{ \AA}$ to the total flux within $3750 \text{ \AA} < \lambda < 3950 \text{ \AA}$. These ranges include all the absorption lines.

All the wavelength ranges are in the rest-frame of the object. For spectra for which no redshift could be determined we only estimated the global S/N assuming the cluster redshift $z=0.395$.

3.4. The catalogue

An excerpt from the final catalogue is shown for reference in Table 4, the full catalogue is available in electronic form at the Centre de Données Stellaires (CDS)⁴. All entries from the catalogue are marked with their redshifts in Figs. 4a–4h.

In detail the contents of Table 4 are as follows:

Column 1: Object number. The catalogue is sorted by relative right ascension (Column 2).

Column 2/3: Right ascension and declination relative to $\alpha=00^{\text{h}}26^{\text{m}}35^{\text{s}}70$, $\delta=17^{\circ}09'43''06$ (J2000), given in arcsec.

Column 4: Redshift.

Column 5: Redshift reliability code: A = “secure”, B = “probable”, C = “possible”, D = “uncertain”, S = “star”. For objects taken from Dressler et al. (1999) and not observed by us, we give their quality code (ranging from 1 to 4).

Column 6: V magnitude (SExtractor MAG_BEST), from CFH12k image.

Column 7: $V-I$ colour, measured in 14 pixel ($2''/8$) diameter apertures from the CFH12k (V) and UH8k (I) images. Occasionally I magnitudes (and hence $V-I$ colour) are not available due to the object falling on a gap between two chips of the UH8k (see Sect. 2.1).

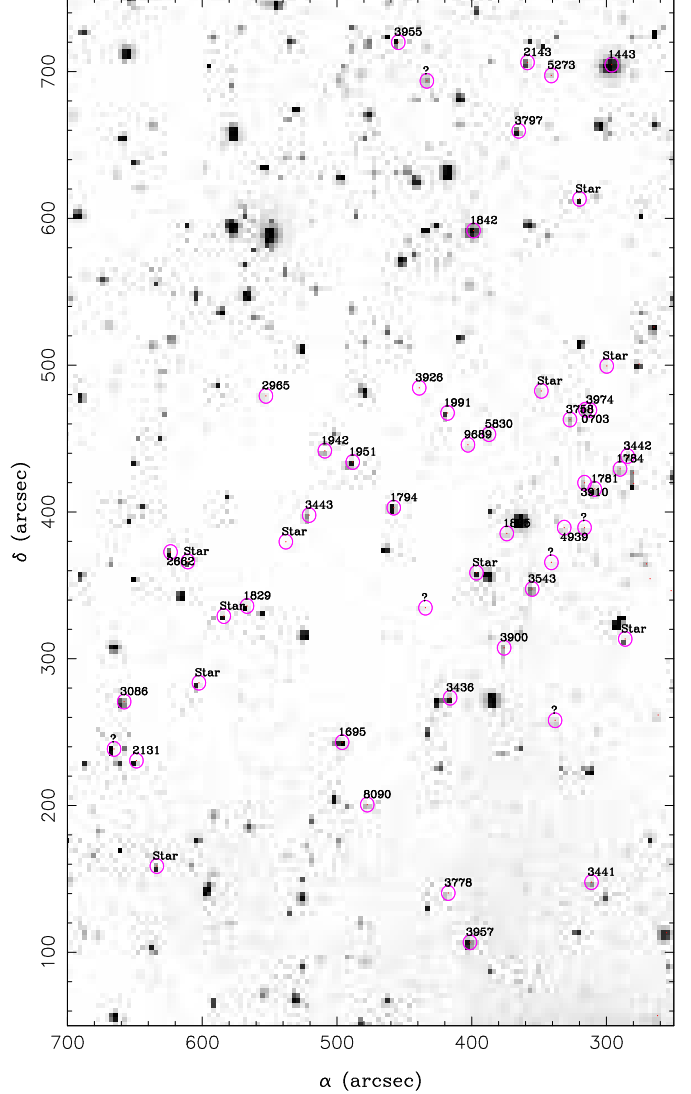


Fig. 4a. Subsections of the CFH12k V-band image with redshifts for members of the spectroscopic sample. The positions of the subsections on the whole field are marked in Fig. 1. For redshifts $z < 1$ only the decimals are given; for galaxies marked “?” spectra are available but no redshift could be determined. The (electronic) catalogue (cf. Table 4) is sorted by relative right ascension, so the entry for any object can be easily identified by noting its coordinates.

Column 8: [O II] λ 3727 equivalent width (in Å). The error was estimated using Eq. 2. We use the convention that equivalent widths are positive for emission and negative for absorption lines. For objects taken from Dressler et al. (1999) and not observed by us, we remeasured the equivalent widths ourselves from their spectra, so as to provide homogeneous equivalent width measurements.

Column 9: [O III] λ 5007 equivalent width (in Å).

Column 10: H α equivalent width (in Å).

Column 11: H β equivalent width (in Å). **XS Column 12:** H δ equivalent width (in Å). The error was estimated using Eq. 2.

Column 13: Strength of the 4000 Å break.

⁴ <http://cdsweb.u-strasbg.fr/cats/J.A+A.htx>

Table 4. The catalogue. This table presents a selection from the sample, the full catalogue is available in electronic form at CDS. The first seven entries correspond to the example spectra shown in Fig. 2. The next seven/six entries belong to the northern/southern groups at $z \sim 0.495$, discussed in Sect. 4. Finally we list several objects in the vicinity of the dark structure detected by Bonnet, Mellier & Fort (1994). See the text for a description of the table contents.

num	R.A.	Dec	z	Q	V	$V - I$	[O II]	[O III]	H α	H β	H δ	4000 Å	S/N	Runs	Lines
531	189.8	414.9	0.3943	A	21.70	1.18	23±3	6	-	4	-4±1	1.1	11.7	2	H/K, H ζ , H η , H θ , [O II]...
221	-117.1	150.3	0.3938	A	20.46	1.73	-	-	-	-	-3±1	1.8	16.9	3, D97	br, H/K, H ζ , H η , H θ ...
80	-366.5	-117.5	0.3944	A	23.46	0.62	77±15	109	-	23	-	1.1	2.3	3	[O II], H β , [O III]
625	376.6	305.8	0.3900	B	21.41	1.47	-	-	-	-	-	1.4	11.0	2	H/K, H δ , H γ , G, H β (ab)
103	-323.9	158.1	0.3963	D	21.88	1.69	-	-	-	-	-	1.7	3.6	3	br
540	206.2	588.7	0.4907	A	21.03	2.48	12±2	-	-	-	-	1.7	10.4	4	G, H β (ab), br, Mg I
378	3.9	-5.6	0.3973	A	22.58	—	78±5	48	-	32	-	1.1	5.9	3	[O II], [O III], H β , H γ (em), H δ (em)...
209	-133.6	596.3	0.4892	A	22.48	1.20	33±2	6	-	10	-	1.4	11.7	3	H θ , H η , H ζ , H β , [O II]...
315	-34.2	559.5	0.4928	A	22.28	1.68	8±1	-	-	4	-	1.5	23.2	3	H/K, H ζ , H η , H θ , H β ...
519	175.1	558.2	0.4912	A	21.32	2.35	10±2	-	-	-	-	1.8	8.1	4	br, G, H θ , H η , NaD...
537	199.7	599.4	0.4951	A	21.37	2.39	-	-	-	-	-	-	5.5	4	H/K, H η , H θ , G
546	216.7	589.7	0.4877	C	21.81	2.33	-	-	-	-	-	1.4	6.3	4	H, H γ , H η
562	240.2	531.6	0.4917	C	20.23	1.24	-	-	-	-	-4±2	1.2	6.4	4	H γ , H δ , G
567	251.0	545.7	0.4980	A	20.30	1.58	10±2	-	-	-	-	1.1	8.7	4	H/K, H ζ , H η , H θ , G...
513	169.4	393.7	0.5016	C	22.98	1.87	21±4	-	-	-	-	1.2	6.2	2	G, H γ , H δ , H/K, H ζ
528	184.6	374.3	0.4969	A	22.24	2.12	1±2	-	-	-	-5±1	1.4	9.5	2	H δ , G, H γ , H β (ab), H θ ...
556	230.6	271.1	0.4955	A	23.47	2.35	-3±2	-	-	-	-	1.7	5.0	2	H/K, H δ , G, H γ , H θ ...
579	268.7	353.6	0.5000	B	23.57	2.04	14±4	-	-	-	-	1.5	5.9	2	H δ , H/K, H θ , H ζ , G
580	271.4	363.7	0.4938	A	21.94	2.28	6±2	-	-	-	-	1.5	9.3	2, 2	H/K, H ζ , H η , G, H β (e+a)...
610	332.6	387.9	0.4939	B	22.45	2.16	20±3	-	-	-	-	1.4	5.1	2	br, [O II]
518	175.0	255.1	0.0000	S	21.78	3.07	-	-	-	-	-	0.0	-	2	NaD, Mg I, bands
542	209.8	261.6	0.2981	A	22.34	0.97	31±11	9	12	-	-	1.1	9.4	2	[O III], [O II]
544	211.3	243.4	0.1755	B	19.98	1.39	-	-	-	-	-	-	4.7	2	Mg I, Fe I, G, H γ , br...
552	226.9	245.0	0.3935	A	23.02	1.09	53±8	19	-	-	-5±2	1.1	4.8	2	[O II], H β , [O III], G, H γ (em)...
563	240.6	256.7	0.3797	A	20.56	1.61	8±1	-	-	3	-3±1	1.4	21.7	2, 2	H/K, H ζ , H η , H θ , [O II]...
566	246.2	279.9	0.4000	A	21.49	1.63	-	-	-	-	-5±1	1.4	10.2	2	H/K, H δ , G, H γ , H β (ab)...
576	262.0	260.8	0.3911	A	21.86	1.77	-	-	-	-	-	1.6	12.4	2	br, H/K, H θ , H ζ , H η ...
...

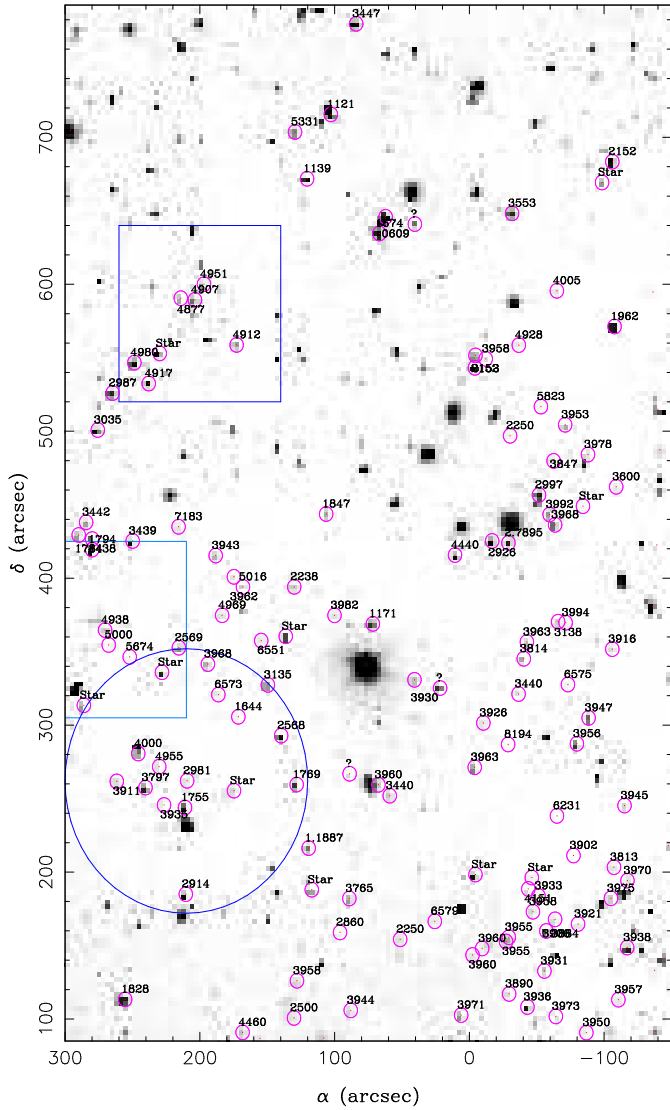


Fig. 4b. Continued. The squares mark the positions of Figs. 9, the circle the area around the weak shear signal detected by Bonnet, Mellier & Fort (1994), discussed in Sect. 4.

Column 14: Signal-to-noise ratio measured between 4050 and 4250 Å.

Column 15: Number(s) of the observing run(s) during which the object was observed (cf. Table 1). Objects observed by Dressler et al. (1999) are marked by “D” and the number from their catalogue.

Column 16: Lines that could be identified in the spectrum/spectra.

We provide new spectra for 618 objects, of which 581 have redshifts. The global success rate is therefore 94%. Not all redshifts are equally secure though: We qualify 435 of our redshifts (70%) as “secure” (quality code A), 28 (5%) as “uncertain” (code D) and 86 (14%) of intermediate quality. 34 objects (5%) turned out to be stars. The fraction of “secure” redshifts is 83% for foreground galaxies at $z < 0.37$, 82% for galaxies around the cluster

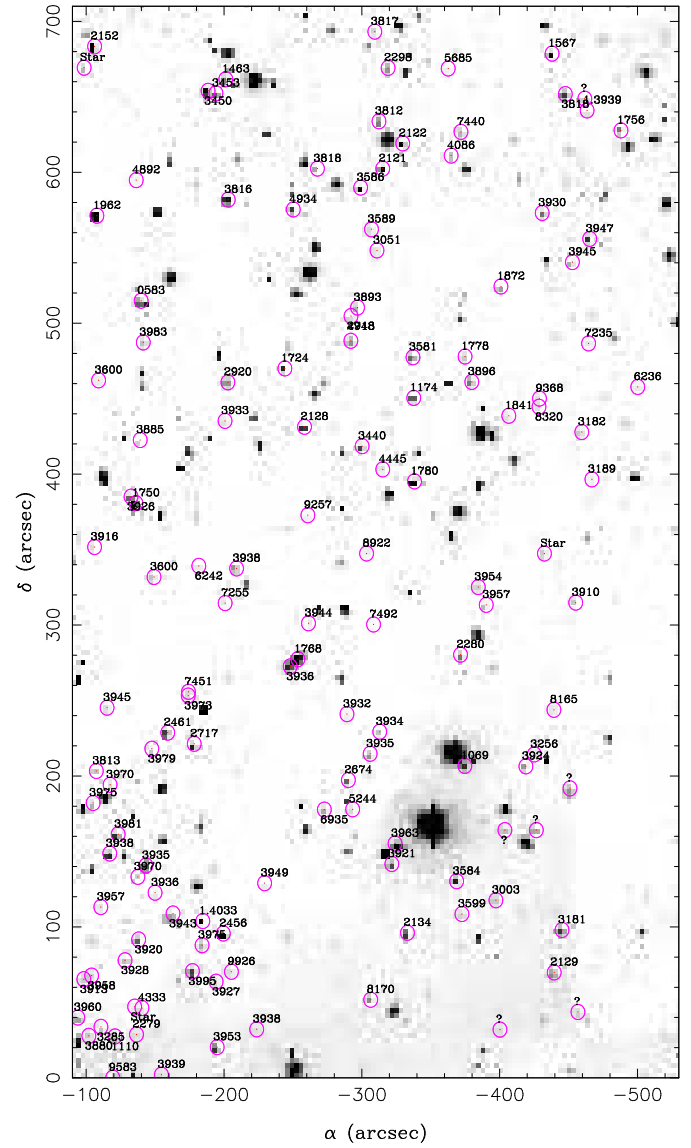


Fig. 4c. Continued

redshift ($0.37 < z < 0.41$), and drops to 53% for galaxies at higher redshift.

For completeness, we include in the catalogue the redshifts provided by Dressler et al. (1999). The corresponding entry number from their catalogue (prefixed by ‘D’) is listed in column 15 of our catalogue. The catalogue as published by Dressler et al. (1999) contains 130 entries, of which 107 are cluster members. However, we noticed several errors in their catalogue, reducing the number of distinct objects to 125⁵. 54 of these objects were observed by us as well, usually with concordant redshifts, see the discussion in Sec. 3.2 and Fig. 3. There were however five problematic cases: Dressler et al. give the redshift for object 376 (D7) as 0.3755, whereas our spectrum indicates

⁵ Dressler et al. (1999) failed to make several identifications within their sample: thus D19 and D66 seem to be the same object, as are D21 and D65, D113 and D120, D122 and D125, D22 and D73.

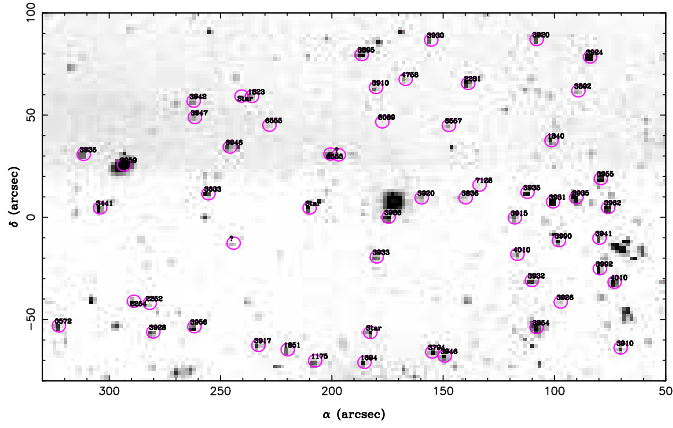


Fig. 4d. Continued

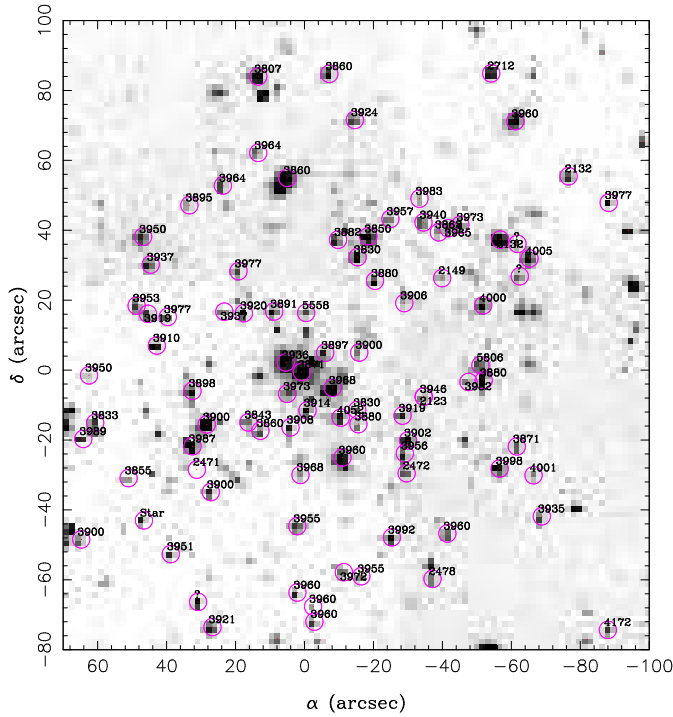


Fig. 4e. Continued

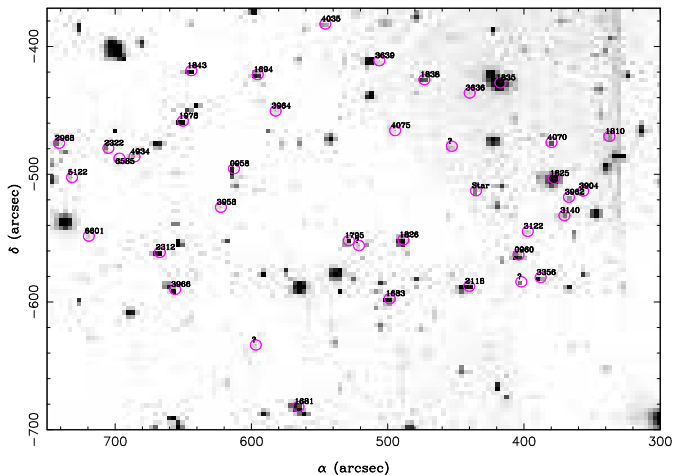


Fig. 4f. Continued

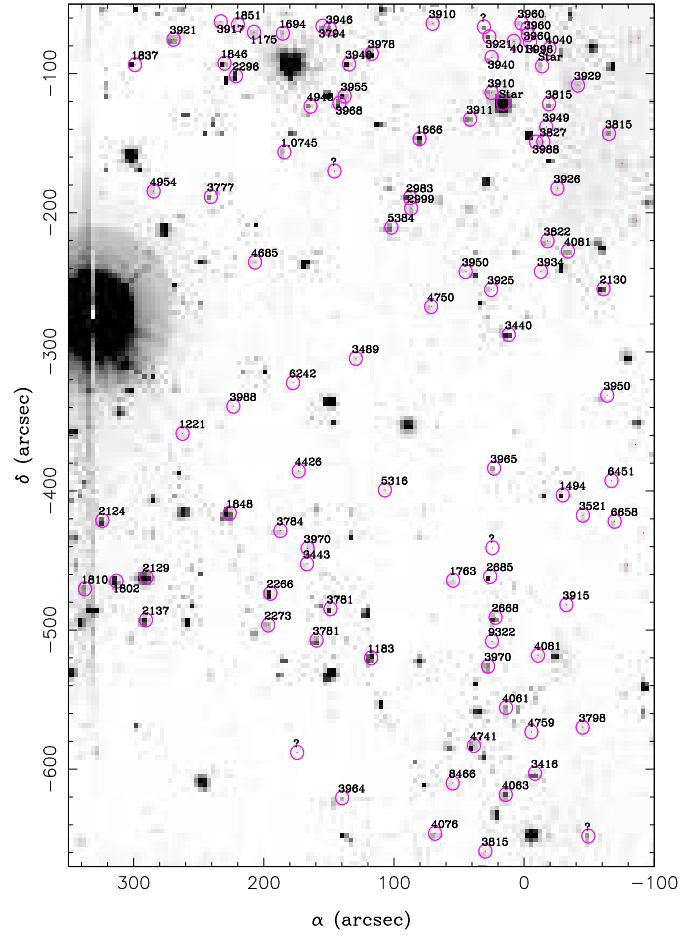


Fig. 4g. Continued

a secure 0.3955. We assume that this is a typographical error in the Dressler et al. list and adopt our value. Our spectrum for object 416 (D33) indicates $z = 0.3895$ as opposed to their 0.4035. Since Dressler et al. only give this a quality code ‘3’, we adopt our value. Object 289 (D109) is similarly uncertain. Object 466 should be identical to Dressler et al.’s object D37, however the spectra are completely different giving secure redshifts of 0.3916 and 0.1840 respectively. We have to assume therefore that D37 has wrong coordinates. A similar problem occurs for D130 (our 237).

Adding the 69 objects which were observed by Dressler et al. alone increases the size of the catalogue to 687 objects, with 650 identified redshifts.

3.5. Completeness

Fig. 5 presents colour-magnitude diagrams (CMDs) for the photometric (for the overlap region of the CFH12k and UH8k images) and the spectroscopic catalogues. For the latter catalogue we also show separate CMDs for foreground galaxies at $z < 0.37$, background galaxies at $z > 0.41$, galaxies at the cluster redshift ($0.37 < z < 0.41$) and for a newly identified group of galaxies at $z = 0.495$ (see Sect. 4).

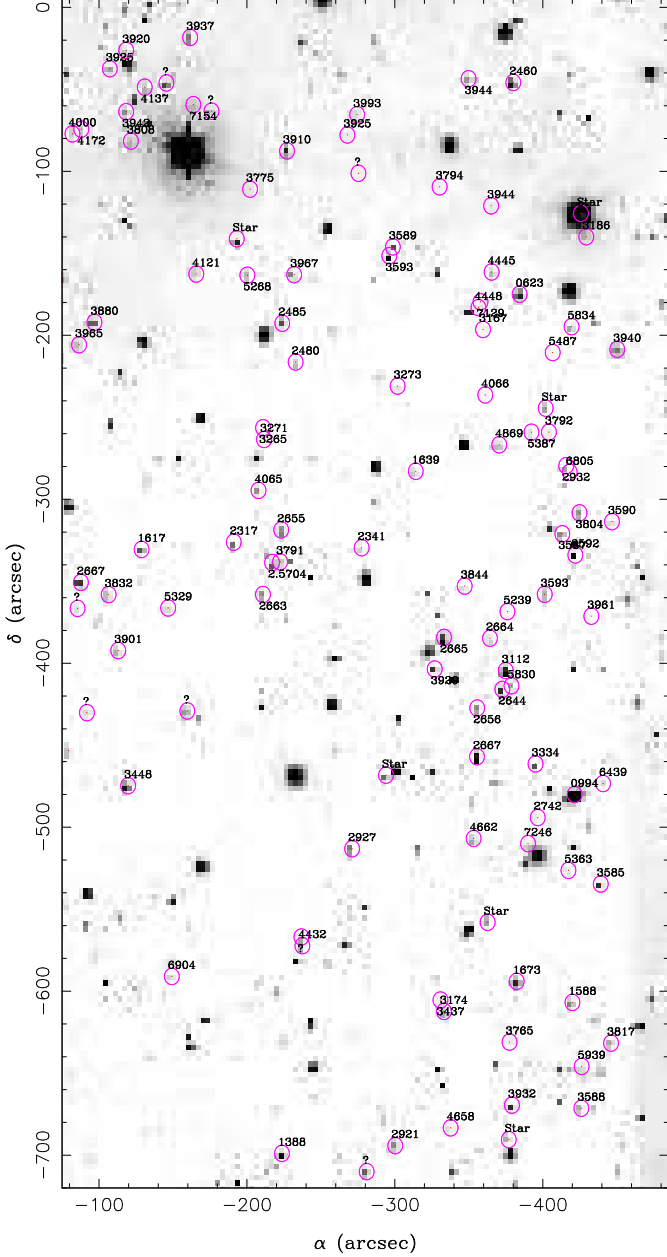


Fig. 4h. Continued

The primary criterion for the candidate selection for the spectroscopic survey was $V < 23$. The completeness in V magnitude of the final catalogue is shown in Fig. 6, where for each galaxy from the spectroscopic catalogue we count the number of objects in a bin of ± 0.25 mag around the galaxy magnitude in both the spectroscopic and photometric catalogues (the latter restricted to the survey area as outlined in Fig. 7) and define their ratio as the total completeness at the given magnitude. Between $V \simeq 20$ and $V \simeq 22$ the completeness is roughly constant at $\sim 45\%$ and drops rapidly for fainter magnitudes. Restricting the same analysis to the central area within $3'$ of the cluster centre (using larger bins of ± 0.5 mag) shows that in this region the completeness exceeds 80% between $V \simeq 20$ and $V \simeq 22$.

A visual impression of the variation of the completeness across the survey area is given in Fig. 7 where we use an adaptive top-hat (its radius at any given point of a grid is the geometric mean of the distances to the 10th and 11th nearest objects with spectroscopy) to compute the ratio of the numbers of objects with spectroscopy (fixed to 10) and the number of objects in the photometric catalogue. In order to have samples with well-defined (though *a posteriori*) photometric selection limits we restrict the spectroscopic and photometric catalogues for this purpose to subsamples with $20 < V < 23$ and $0.6 < V - I < 2.4$. As Fig. 5 shows, this region of the colour-magnitude plane encloses virtually all the cluster members in the spectroscopic catalogue. Within our restricted sample the separation between stars and galaxies within the photometric catalogue is fairly straightforward using SExtractor's CLASS_STAR parameter. Within a total of 2722 objects we find 312 stars (with an error of about ± 10 due to ambiguous cases) or 11.5% . Since useful shape information was not available for the preparation of all the spectroscopic observing runs (about 5% of the objects in the spectroscopic catalogue are stars), the whole photometric sample is used in Fig. 7. The completeness values are therefore actually *underestimates* if interpreted as completeness for spectroscopic coverage of *galaxies* alone. The cluster centre is sampled at $> 70\%$ completeness in a region of about $80'' \times 150''$.

4. Discussion

The three-dimensional distribution of the galaxies in the redshift sample is shown in Fig. 8 in the form of wedge diagrams, where the angular position of each object on the sky has been converted to proper distance from the line of sight, appropriate for the given redshift in a $\Omega_M = 1$, $\Omega_\Lambda = 0$ world model. The cluster Cl0024+1654 shows up clearly as a sheet at $z \simeq 0.4$. The expanded views show that Cl0024+1654 is not a simple isolated cluster but that there is a foreground “clump” at $z = 0.38$, superimposed onto the main cluster and connected to the latter via a narrow bridge. In a companion paper (Czoske et al. 2001) we discuss an interpretation of this structure as being due to the foreground cluster having passed through the main cluster.

We find a pair of compact groups of galaxies at $z = 0.495$ about $10'$ to the north-east of the centre of Cl0024+1654 (see Fig. 8 at $x \simeq 1$ Mpc, $y \simeq 2$ Mpc). The northern group includes 8 galaxies, centered at $574''$ north and $203''$ east of the cluster centre, the southern group includes 6 galaxies centered at $369''$ north and $250''$ (median positions); the projected distance between the groups is thus $\sim 740 h^{-1}$ kpc. The mean redshifts are $\bar{z}_N = 0.4921$ and $\bar{z}_S = 0.4970$, the formal velocity dispersions $\sigma_N = 657 \text{ km s}^{-1}$ and $\sigma_S = 647 \text{ km s}^{-1}$. Student's t -test rejects the hypothesis that the two groups have the same mean redshift at 99% confidence, so we assume that we are really seeing two separate groups. The velocity dis-

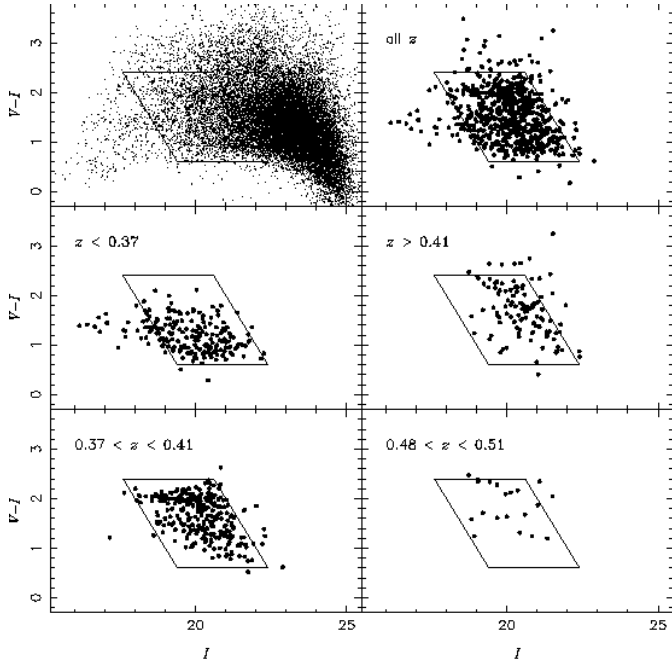


Fig. 5. $V-I$ colour-magnitude diagrams. The top-left diagram shows the full photometric catalogue, the top-right diagram the full spectroscopic catalogue. The next three diagrams split the spectroscopic catalogue according to redshift, showing foreground and background galaxies as well as galaxies around the cluster redshift $z \sim 0.39$. Note the clearly visible cluster sequence at $V-I \simeq 2$ in the latter diagram. The bottom-right diagram shows the members of the newly discovered group of galaxies at $z \sim 0.495$ (see Section 4). The parallelogram marks the subsample used in the completeness map (Fig. 7), $20 < V < 23$, $0.6 < V-I < 2.4$.

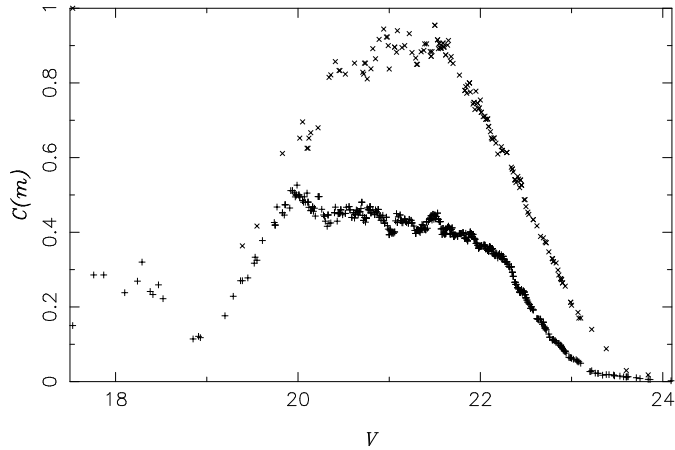


Fig. 6. Completeness of the spectroscopic survey in V magnitude. For each galaxy from the catalogue this is given as the ratio of the numbers of galaxies in the spectroscopic and photometric catalogues in a given bin width centered on the magnitude of the galaxy. Pluses mark galaxies taken from the whole survey area (as outlined in Fig. 7), crosses galaxies within $3'$ of the cluster centre. In the former case, a bin width of 0.5 mag was used, in the latter a bin width of 1 mag.

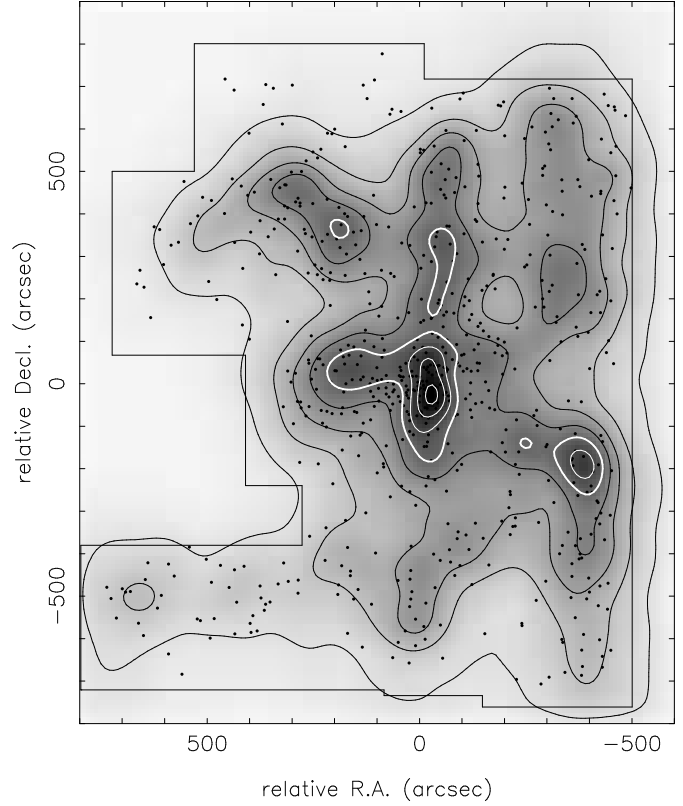


Fig. 7. Map of the completeness variation of the spectroscopic catalogue as gray-scale with overlaid contours. The completeness at any point is determined in a circular top-hat encompassing the 10 nearest neighbours in the spectroscopic survey; the map is smoothed with a Gaussian of width $30''$. Contour lines are spaced in 10% steps. The 50% contour is marked by a bold line, contours at less than 50% are drawn in black, higher contours in white.

persions are presumably enhanced by tidal interaction between the groups.

Fig. 9 shows colour images of the northern and southern groups created from the I- and V-band CCD images. The galaxy at $z = 0.4907$ is surrounded by three objects of similar, blue colour. It is tempting to interpret this group as multiple images of the same background object. In this case, using the curvature radius ($\sim 5''$) as an estimate for the Einstein radius and $z_s = 1$ as a rough guess for the redshift of the background source, we obtain $5.8 \times 10^{12} h^{-1} M_\odot$ for the mass within this radius.

Another overdensity in Fig. 8 occurs at $z \sim 0.18$. These galaxies are however distributed fairly uniformly across the field with no obvious spatial concentration and are therefore just part of the general large-scale structure in the Universe.

In the first detection of a coherent shear field around a cluster of galaxies, Bonnet et al. (1994) found a signal to the north-east of the centre of Cl0024+1654, indicating a concentration of mass at a point where no overdensity of galaxies is apparent in the two-dimensional images. The direction to this dark “clump” is indicated by a circle in

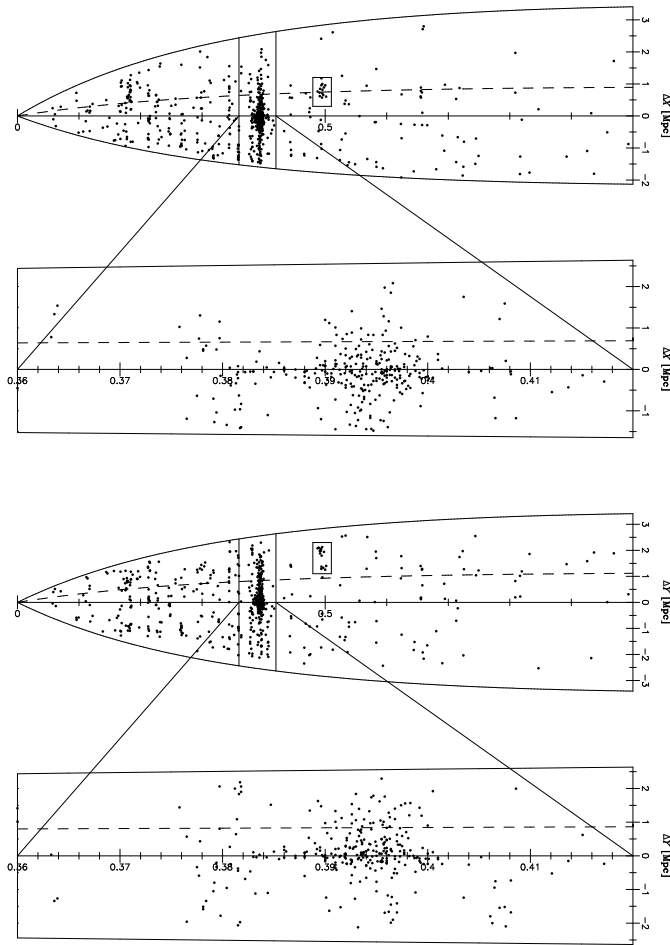


Fig. 8. Three-dimensional distribution of the objects in our redshift catalogue. In the two upper panels the objects are projected onto the right ascension axis, in the lower two onto the declination axis. The upper panel of each pair shows the large-scale distribution from $z=0$ to $z=1$, the lower panel an expanded view of the environment of the cluster Cl0024 itself. The dashed line marks the direction towards the potential perturbation detected by Bonnet et al. (1994). Two groups at $z \sim 0.495$ are marked by rectangles. The conversion from angular position on the sky to proper transverse distance was done assuming an Einstein-de Sitter Universe with $H_0 = 100 \text{ km s}^{-1} \text{ Mpc}^{-1}$.

Fig. 4b and by the dashed line in Fig. 8. There is no significant over-density along this line which could explain the spatial tightness of the signal observed by Bonnet et al.

5. Conclusions

In this paper we present a catalogue of spectroscopic data for 687 objects in a field of $21 \times 25 \text{ arcmin}^2$ around the centre of the cluster of galaxies Cl0024+1654 at $z \sim 0.395$, 295 of which lie in the vicinity of the cluster itself, in the range $0.37 < z < 0.41$. The completeness of the sample exceeds 80% around the cluster centre for $V < 22$, dropping to $\sim 70\%$ for $V < 23$. The mean completeness over the whole

Fig. 9. “True” colour images of the apparent centres of the northern (top) and southern (bottom) groups of galaxies at $z \simeq 0.49$. The images were created from the V and I band images, the green channel is an average of these two images. Supposed member galaxies of the group are conspicuous by their yellow colour, corresponding to $V - I \sim 2.4$. Note the blue arc-like structure around the galaxy at $z = 0.4907$.

field is about 45% down to $V = 22$. This is therefore one of the largest spectroscopic surveys available for a cluster at $z \gtrsim 0.2$ and the largest at $z \sim 0.4$. Apart from redshifts the catalogue lists photometric data and equivalent widths for five lines as well as the strength of the 4000 \AA break, important for determining present and recent star forming activity. The catalogue represents a unique database for investigations into the structure of a medium-redshift cluster of galaxies and its environment.

We report the discovery of a binary group of galaxies at $z \simeq 0.495$, which includes a gravitational arc candidate. A further overdensity in the redshift distribution at $z \sim 0.18$ can at present not be attributed to a collapsed structure, although we cannot exclude the possibility that a centre for such a structure exists outside the field covered by our survey. None of the structures seen in the redshift distribution seems to be able to explain the coherent shear signal at $\sim 6'$ to the north-east of the projected centre of Cl0024+1654, detected by Bonnet et al. (1994).

The main result of this project is that Cl0024+1654 is not a simple isolated cluster, as has hitherto been assumed in interpreting kinematical, lensing and X-ray data. Instead there is a second, less massive cluster projected onto the centre of the main cluster. The separation of Cl0024+1654 into two components has strong consequences for the interpretation of observational data and should in particular help to resolve the well-known discrepancy between masses determined using different methods for this cluster (Soucail et al. 2000). The structure of Cl0024+1654, a scenario for possible interaction between the main and foreground clusters and the effects of this interaction on the properties of the cluster galaxy populations will be discussed in more detail in the second paper of this series (Czoske et al. 2001). The photometric data obtained in conjunction with this project will be used by Mayen et al. (2001) to investigate the depletion of background objects due to the gravitational lensing effect of Cl0024+1654.

Acknowledgements. OC thanks the European Commission for generous support under grant number ER-BFM-BI-CT97-2471. JPK thanks CNRS for support and acknowledges a European Large Scale Facility grant for the WHT observation. This work was supported by the TMR Network “Gravitational Lensing: New Constraints on Cosmology and the Distribution of Dark Matter”⁶ of the European Commission under con-

⁶ <http://www.ast.cam.ac.uk/IoA/lensnet>

tract No. ER-BFM-RX-CT97-0172. TJB wishes to thank Observatoire Midi-Pyrénées for hospitality.

References

- Abraham, R.G., Smecker-Hane, T.A., Hutchings, J.B., Carlberg, R.G., Yee, H.K.C., Ellingson, E., Morris, S., Oke, J.B., Rigler, M. 1996, *ApJ* 471, 694
- Allington-Smith, J., Breare, M., Ellis, R., Gellatly, D., Glazebrook, K., Jordan, P., Maclean, J., Oates, P., Shaw, G., Tanvir, N., Taylor, K., Taylor, Ph., Webster, J., Worswick, S. 1994, *PASP* 106, 983
- Balogh, M.L., Schade, D., Morris, S.L., Yee, H.K.C., Carlberg, R.G., Ellingson, E. 1998, *ApJ* 504, L75
- Bartelmann, M., Schneider, P. 2001, *Phys. Rep.* 340, 291
- Bertin, E., Arnouts, S. 1996, *A&A* 117, 393
- Bonnet, H., Mellier, Y., Fort, B. 1994, *ApJ* 427, L83
- Broadhurst, T., Huang, X., Frye, B., Ellis, R. 2000, *ApJ* 534, L15
- Butcher, H., Oemler, A. Jr. 1978, *ApJ* 219, 18
- Butcher, H., Oemler, A. Jr. 1984, *ApJ* 285, 426
- Carlberg, R.G., Yee, H.K.C., Ellingson, E., Morris, S.L., Abraham, R., Gravel, P., Pritchett, C.J., Smecker-Hane, T., Hartwick, F.D.A., Hesser, J.E., Hutchings, J.B., Oke, J.B. 1997, *ApJ* 485, L13
- Castander, F.J., Holder, G.P., Clowe, D., Carlstrom, J.E., Schirmer, M., Reese, E.D., Kneib, J.-P. 2000, in: *Constructing the Universe with Clusters of Galaxies (IAP 2000 meeting)*, eds. F. Durret, D. Gerbal
- Cen, R. 1997, *ApJ* 485, 39
- Couch, W.J., Balogh, M.L., Bower, R.G., Smail, I., Glazebrook, K., Taylor, M. 2000, *astro-ph/0010505*, *ApJ* in press
- Cuillandre, J.-C., Luppino, G., Starr, B., Isani, S. 2000, *Proc. SPIE* 4008, 1010
- Czoske, O., Kneib, J.-P., Moore, B., Soucail, G. 2001, in preparation
- Dressler, A. 1980, *ApJ* 236, 351
- Dressler, A., Shectman, S.A. 1987, *AJ* 94, 899
- Dressler, A., Gunn, J.E. 1992, *ApJS* 78, 1
- Dressler, A., Smail, I., Poggianti, B.M., Butcher, H., Couch, W.J., Ellis, R.S., Oemler, A. Jr 1999, *ApJ* 122, 51
- Girardi, M., Giuricin, G., Mardirossian, F., Mezzetti, M., Boschin, W. 1998, *ApJ* 505, 74
- Girardi, M., Mezzetti, M. 2000, *astro-ph/0010302*, *ApJ* in press
- Kassiola, A., Kovner, I., Fort, B. 1992, *ApJ* 400, 41
- Kennicutt, R.C. Jr. 1992, *ApJ* 388, 310
- Kurtz, M.J., Mink, D.J. 1998, *PASP* 110, 934
- Le Fèvre, O., Crampton, D., Felenbok, P., Monnet, G. 1994, *A&A* 282, 325
- Le Fèvre, O., Crampton, D., Lilly, S.J., Hammer, F., Tresse, L. 1995, *ApJ* 455, 60
- Luppino, G., Metzger, M., Miyazaki, S. 1995, *IAU Symposium No. 167*, Kluwer Academic Pub., 297
- Mayen, C., Czoske, O., Soucail, G. 2001, in preparation
- Merritt, D. 1987, *ApJ* 313, 121
- Metzler, C.A., White, M., Loken, C. 2001, *ApJ* 547, 560
- Reblinsky, K., Bartelmann, M. 1999, *A&A* 345, 1
- Schneider, P., Ehlers, J., Falco, E.E. 1992, *Gravitational Lenses*, Springer Verlag, Heidelberg
- Smail, I., Dressler, A., Kneib, J.-P., Ellis, R.S., Couch, W.J., Sharples, R.M., Oemler, A. Jr. 1996, *ApJ* 469, 508
- Soucail, G., Ota, N., Böhringer, H., Czoske, O., Hattori, M., Mellier, Y. 2000, *A&A* 355, 433
- Tyson, J.A., Kochanski, G.P., Dell'Antonio, I.P. 1998, *ApJ* 498, L107
- Yee, H.K.C., Ellingson, E., Carlberg, R.G. 1996, *ApJS* 102, 269
- Yee, H.K.C., Morris, S.K., Lin, H., Carlberg, R.G., Hall, P.B., Sawicki, M., Patton, D.R., Wirth, G.D., Ellingson, E., Shepherd, C.W. 2000, *ApJS* 129, 475
- Zwicky, F., Herzog, E., Wild, P., Karpowicz, M., Kowal, C.T. 1965, *Catalogue of Galaxies and of Clusters of Galaxies*, California Institute of Technology, vol. 5

This figure "figure9_N.jpg" is available in "jpg" format from:

<http://arxiv.org/ps/astro-ph/0103123v1>

This figure "figure9_S.jpg" is available in "jpg" format from:

<http://arxiv.org/ps/astro-ph/0103123v1>